

Degradation of myocardial perfusion SPECT images caused by contaminants in thallous (^{201}Tl) chloride

Steven G. Staelens · Tim C. de Wit ·
Ignace A. Lemahieu · Freek J. Beekman

Received: 25 July 2007 / Accepted: 4 January 2008 / Published online: 25 January 2008
© Springer-Verlag 2008

Abstract

Purpose Thallous (^{201}Tl) chloride is a single-photon emission computed tomography (SPECT) tracer mainly used for assessing perfusion and viability of myocardial tissue. ^{201}Tl emits X-rays around 72 keV and gammas at 167 keV, and has a half-life of 73 h. Regulations allow an intrinsic contamination up to 3–5%, which is mainly caused by ^{200}Tl (368 keV; 26 h) and by ^{202}Tl (439 keV; 12.2 days). Contra-intuitive to the low-level percentages in which these contaminants are present, their impact may be significant because of much higher gamma camera sensitivity for these high-energy photon emissions. Therefore, we investigate the effects of the contaminants in terms of detected

fractions of photons in projections and contrast degradation in reconstructed images.

Methods Acquisitions of a digital thorax phantom filled with thallous (^{201}Tl) chloride were simulated with a validated Monte Carlo tool, thereby, modelling 1% of contamination by ^{200}Tl and ^{202}Tl each. In addition, measurements of a thorax phantom on a dual-headed gamma camera were performed. The product used was contaminated by 0.17% of ^{200}Tl and 0.24% of ^{202}Tl at activity reference time (ART). This ART is specified by the manufacturer, thereby, accounting for the difference in half-lives of ^{201}Tl and its contaminants. These measurements were repeated at different dates associated with various contamination levels.

Results Simulations showed that, with 1% of ^{200}Tl and ^{202}Tl , the total contamination in the 72 keV window can rise up to one out of three detected photons. For the 167keV window, the contamination is even more pronounced: more than four out of five detections in this photopeak window originate from contaminants. Measurements indicate that cold lesion contrast in myocardial perfusion SPECT imaging is at maximum close to ART. In addition to a higher noise level, relative contrast decreases 15% 2 days early to ART, which is explained by an increase in ^{200}Tl contamination. After ART, contrast decreased by 16% when the ^{202}Tl contamination increased to the maximal allowed limit.

Conclusions Contra-intuitive to the low-level percentages in which they are typically present, penetration and down-scatter of high-energy photons from ^{200}Tl and ^{202}Tl significantly contribute to thallous (^{201}Tl) chloride images, thereby, reducing contrast and adding noise. These findings may prompt for improved production methods, for updated policies with regard to timing of usage, and they also render the usefulness of adding the high photopeak window (167

S. G. Staelens · T. C. de Wit · F. J. Beekman
Department of Nuclear Medicine, Image Sciences Institute,
University Medical Center Utrecht,
Utrecht, The Netherlands

S. G. Staelens · T. C. de Wit · F. J. Beekman
Department of Pharmacology and Anatomy,
Rudolf Magnus Institute of Neuroscience,
University Medical Center Utrecht,
Utrecht, The Netherlands

F. J. Beekman
Department of Applied Sciences,
Delft University of Technology,
Delft, The Netherlands

S. G. Staelens · I. A. Lemahieu
Department of Medical Imaging and Signal Processing,
Ghent University–IBBT,
Ghent, Belgium

S. G. Staelens (✉)
Ghent University–IBBT, IBITECH-MEDISIP,
De Pintelaan 185, Block B-502a,
B-9000 Ghent, Flanders, Belgium
e-mail: Steven.Staelens@ugent.be

keV) questionable. A window-based correction method for this contamination is advisable.

Keywords Myocardial perfusion · Septal penetration · Impurities · Monte Carlo · Thallium

Introduction

Thallous (^{201}Tl) chloride is amongst the most commonly used perfusion agents for myocardial perfusion SPECT (MPS with SPECT: single-photon emission computed tomography) imaging [1]. Unlike several $^{99\text{m}}\text{Tc}$ -based perfusion agents, the unique redistribution property has made thallous (^{201}Tl) chloride SPECT a consistently effective modality for identifying myocardial viability and guiding appropriate patient management. Despite the ongoing debate whether $^{99\text{m}}\text{Tc}$ -labelled perfusion agents should or could replace thallous (^{201}Tl) chloride for MPS, 60% of the MPS studies performed yearly in the USA in the late 1990s used thallous (^{201}Tl) chloride [2]. A similar scale of thallous (^{201}Tl) chloride usage was also found by a more recent survey in the UK [3]. Therefore, improving the image quality for thallous (^{201}Tl) chloride MPS remains clinically important.

Thallous (^{201}Tl) chloride is cyclotron produced and typically contains, next to ^{201}Tl , contaminations by ^{200}Tl , ^{202}Tl and, to a much lower extent, ^{203}Pb (cf. Table 1). These contaminations are inherent to the production process that is based on indirect nuclear reactions on natural and enriched thallium such as $^{203,205}\text{Tl}(p,3n/5n) \rightarrow ^{201(\text{m} + \text{g})}\text{Pb} \rightarrow ^{201}\text{Tl}$ [4]. The level of contaminations are dictated by several factors: (1) the occurring nuclear reactions ($^{203}\text{Tl}(p,2n) \rightarrow ^{202\text{m}}\text{Pb} \rightarrow ^{202}\text{Tl}$ or $^{203}\text{Tl}(p,4n) \rightarrow ^{200}\text{Pb} \rightarrow ^{200}\text{Tl}$), (2) the enrichment of the irradiated target (typically $> 90\%$ ^{203}Tl , rest ^{205}Tl), (3) the incident projectile energy (higher energy causes more ^{200}Tl , lower energy causes more ^{202}Tl), (4) the energy loss in the target, (5) the radiochemical separation process (repeated separations causes relatively more ^{200}Tl and less ^{202}Tl) and, finally, (6) the irradiation, cooling, storage and waiting times (short waiting time after first separation causes more ^{202}Tl , whereas waiting long causes

more ^{200}Tl). The level of contaminations can be determined both accurately and fast using gamma-spectrometry [5]. These contamination levels can be reduced by using a production based on a direct nuclear reaction such as $^{202}\text{Hg}(p,2n)$ on an enriched ^{202}Hg target [5]. It is, however, evident that producing thallous (^{201}Tl) chloride with higher radionuclide purity would sharply decrease the production yield, increasing the unit cost of the radiopharmaceutical compound.

The aforementioned contamination levels are regulated according to the US Pharmacopoeia [6] stating that not less than 95% of the total activity should be present as ^{201}Tl and not more than 2.0% of ^{200}Tl , 0.3% of ^{203}Pb and 2.7% of ^{202}Tl is allowed. The European and British Pharmacopoeia are more strict [7, 8] stating that not less than 97% of the total activity should be present as ^{201}Tl and that no more than 2.0% of ^{202}Tl is allowed. On average, the production batches of the main manufacturers maintain a safe margin as their internal requirements are often more restrictive.

As shown in Fig. 1, the different decay constants (Fig. 1a) cause the impurity contamination percentages to vary significantly over time (Fig. 1b). It is, therefore, necessary to allow sufficient time to elapse between preparation of thallous (^{201}Tl) chloride and its use, to permit the level of ^{200}Tl to decay to an acceptable level. On the other hand, the presence of ^{202}Tl causes the material to be less suitable for use several days after the activity reference date (ART). This ART is calculated during the production process as the envisaged moment of usage, thereby, accounting for the differences in half-lives of ^{200}Tl , ^{201}Tl , ^{202}Tl and ^{203}Pb when specifying the impurity level. Figure 2 shows the measured energy spectrum of a thallous (^{201}Tl) chloride solution with 2.7% ^{202}Tl contamination (US limit) as acquired on a dual-headed gamma camera with low-energy high-resolution (LEHR) collimators. Normally, in clinical practice, only the range from 0 to 200 keV is shown, but the reason of the bias is more obvious when the energy scale is extended as illustrated here by Fig. 2.

The impact of these contaminants has already been demonstrated in dosimetry where they can make up to 20% of the total dose in certain organs [9]. The total dose increase for a 2% contamination by ^{202}Tl is already 11% [10]. Also, a long-term retention and excretion after myocardial perfusion imaging was concluded because of these contaminants [11]. Recently, Stabin and Brill [12] emphasised that underestimating these contaminants could have influenced thallium dosimetry publications for the past two decades.

Because of the fact that the gamma camera sensitivity for the high-energy photons of these contaminants is two orders of magnitude larger as for the two photopeaks of interest, the impact of the contaminants may also be significant for imaging, contra-intuitive to the low-level

Table 1 Constituents of thallous (^{201}Tl) chloride

Isotope	Main emission peak(s) (keV)	Branching ratio (%)	Half-life (h)
^{201}Tl	X-rays around 70 Gammas at 167	73 10	73
^{200}Tl	368	87	26
^{202}Tl	439	91	294
^{203}Pb	279	81	52

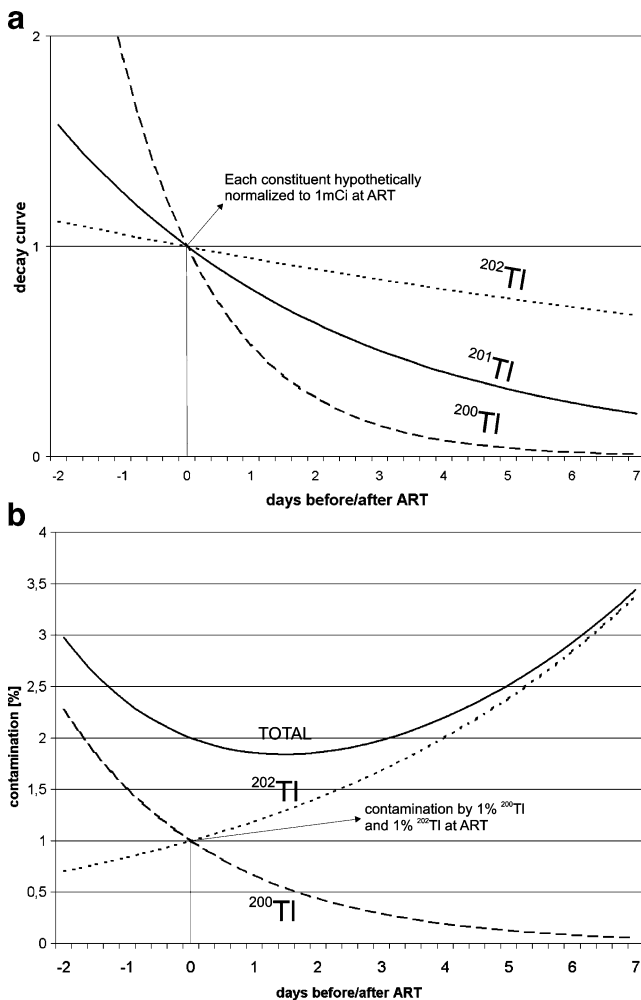


Fig. 1 **a** Radioactive decay rates of ^{201}Tl and its main contaminants and **b** time evolution of ^{201}Tl contamination level with 1% of ^{200}Tl (.....) and 1% of ^{202}Tl (.....) initial contamination at activity reference time (ART). The total contamination (—) has a minimum because of the differences in half-lives of the contaminants

percentages in which they are present. Accordingly, the main goal of this paper is to evaluate the particular impact of contaminants on thallous (^{201}Tl) chloride gamma camera imaging in nuclear medicine. Early analysis of this phenomenon [13, 14] was hampered, as it is very difficult to measure the separate contributions from the different isotopes simultaneously. However, since 3–5 years general purpose Monte Carlo simulators [15–17], originating from high energy physics research, are made suitable for SPECT and are validated with measurements. This manuscript reports for the first time on the usage of such a simulator to quantify the impact of the aforementioned contaminations in MPS imaging. In addition to these simulations, we performed thorax phantom measurements at different thallous (^{201}Tl) chloride shelf lives associated with various contamination levels.

Materials and methods

In this section, we first report on the study performed to validate the Monte Carlo simulator at hand for the task of ^{201}Tl imaging. Next, the simulations that predict the impact of the contaminants are described. Also, several parameters, such as collimator type and patient size, are elucidated using Monte Carlo simulations. Finally, the thorax phantom measurements performed to determine the contrast deterioration are depicted.

Validation of Monte Carlo simulator

The simulator at hand, GATE (Geant4 Application for Tomographic Emission), was designed as a higher level interface for the geometry and tracking (Geant4) nuclear physics code and was adapted for use in nuclear medicine [18]. GATE has been validated extensively by measurements with various isotopes and collimators [19–21]. Additionally for this study, simulations were performed wherein the parameters mimicked the measurements described hereafter, thereby, including all detector parts as well as the phantom table. The collimator was realistically modelled, and simulations included X-ray tracks down to 20 keV.

A measurement of a line source (1 mm radius and 1 cm height) filled with 1 mCi of Tl was performed on a Philips MCD camera mounted with VXHR collimators. The latter collimators have a 2.03-mm hexagonal hole size with

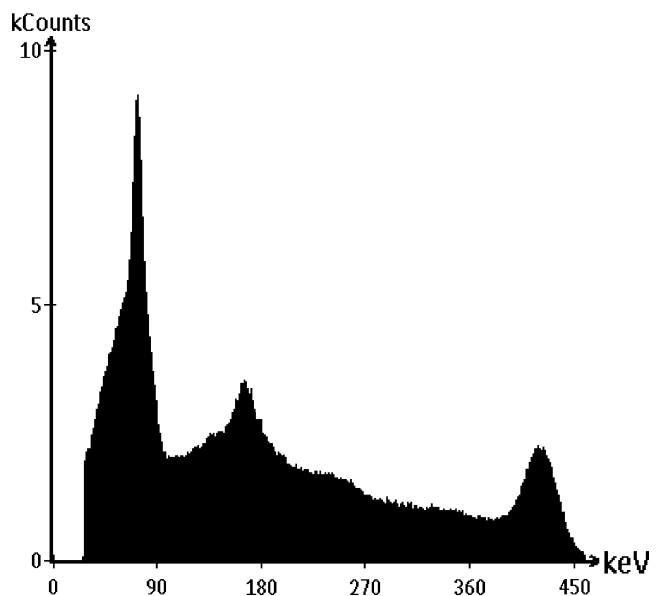


Fig. 2 Measured gamma camera spectrum of a thorax phantom acquired on high-resolution collimators and filled with ^{201}Tl contaminated with 3% ^{202}Tl and no ^{200}Tl (US limit). Note that this spectrum is plotted versus an energy scale that is extended beyond the clinical settings (0–200 keV) to better illustrate the origin of the bias under the ^{201}Tl photopeaks of interest

54-mm hole length and a septal thickness of 0.152 mm. The activity contamination of the thallos (^{201}Tl) chloride source was determined in the production plant of the manufacturer using a high accuracy spectral analyser and was determined to be 1.9 kBq ^{200}Tl and 2.25 kBq ^{202}Tl per MBq ^{201}Tl at ART. The energy spectrum in air was acquired at ART on the gamma camera according to the NEMA-2001 protocol. The translation from channel number to energy was calibrated using three different isotopes (^{153}Gd , ^{57}Co and $^{99\text{m}}\text{Tc}$). Furthermore, the line spread function (LSF) in air at a 15-cm distance from the collimator was measured for a continuous 600 s, and 20% photopeak windows were set around 72 and 167 keV. The LSF is acquired on a 128×128 grid (4.72 \times 4.72 mm) and normalised to its maximum.

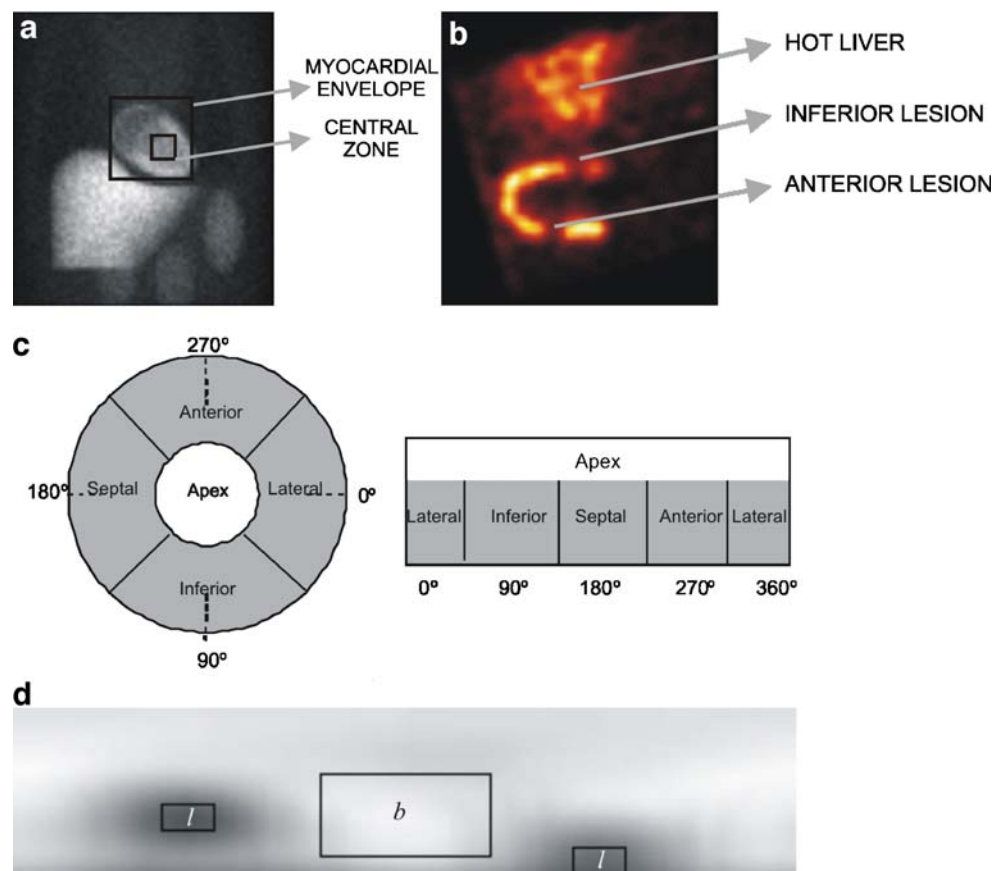
Simulations of a digital thorax phantom

To predict the potential impact of contaminations, a projection of a digital thorax phantom [22] was simulated with GATE. An acquisition of a realistic 4 mCi activity distribution was simulated for 25 s with a model of the Philips Forte system using LEHR collimators (1.4-mm hexagonal hole size, 32.8-mm hole length, 0.152-mm septal thickness). Contamination levels were set to 1% of ^{200}Tl

and ^{202}Tl and 0.25% ^{203}Pb at ART. The lateral and anterior–posterior dimensions of the attenuation map were 42 by 28 cm, and the center of the phantom was positioned at 28 cm from the collimator. The activity concentration ratio of myocardium to liver to background to lungs was set to 100:69:9:3, and the emission map was voxelised in a $64 \times 64 \times 64$ grid (6.34 \times 6.34 mm). The detector active area was 50.8 \times 38.1 mm and was binned on a 128×128 grid (4.72 \times 4.72 mm). Two 20% photopeak windows were defined at 72 and 167 keV. The detected level of contamination was evaluated in three different regions as shown in Fig. 3a: firstly, a central zone of 2×2 pixels; secondly, an envelope for the myocardium of 12×12 pixels delineated on the frontal projection and, thirdly, the full active detector area. The aforementioned simulation study at ART was repeated for a virtual start time of 3 days after ART, being half of the thallos (^{201}Tl) chloride shelf-life.

Additionally, the influence of several parameters is investigated. The simulated acquisitions are repeated for low-energy general purpose (LEGP) collimators, which have a 1.4-mm hexagonal hole size, 24.7-mm hole length and 0.180-mm septal thickness. Also, the influence of patient size is investigated by increasing the lateral and anterior–posterior dimensions of the attenuation map to 46 by 32 cm.

Fig. 3 Methodology: **a** Source positions of all detections in a simulated frontal projection; illustration of the delineation for the central zone and the myocardial envelope; **b** illustration of the two solid defect on an example reconstructed vertical long axis view; **c** generation of circumferential planes—illustration of the spherically sampled apex and cylindrically sampled myocardial wall, and the corresponding sampling angles on a typical Bull’s-eye image; **d** delineation of the defect and reference regions on a circumferential plane



All simulations were performed on a cluster based on openMosix and consisting of 38 nodes with 17 dual XEON 2.4 Ghz processors and 21 dual XEON 2.8 Ghz processors, each with 2 GB memory.

Measurements

Because it is very difficult at production level to vary the contamination for individual batches, we performed repetitive measurements on clinically available thallous (^{201}Tl) chloride at different days to obtain a range of realistic contamination levels. The latter are listed in Table 2, whereas the level of ^{203}Pb was too low to be measurable. The acquisition schedule started from 2 days before ART, at ART, 4 days after ART (half shelf-life), 7 days past ART (end of shelf-life) and up to 15 days after ART (where the ^{202}Tl contamination reaches the US limit).

In these measurements, the thallous (^{201}Tl) chloride was distributed in a large anthropomorphic thorax (model ECT/TOR/P, Data Spectrum Corp., Hillsborough, NC, USA). The lateral and anterior–posterior sizes of the large phantom were 38 and 26 cm, respectively. The phantom configuration comprised a cardiac insert (model ECT/CAR/I) representing the left ventricle, two lung inserts, a liver insert, and a spine insert. Two solid defects (2 ml each) with zero activity were placed in the anterior and inferior walls of the cardiac insert as illustrated on Fig. 3b for an example reconstructed vertical long axis view. The relative activity concentration ratio myocardium/liver/lungs/background was 43:19:1:2, which reflects the distributions encountered in clinical ^{201}Tl studies [23, 24]. Absolute activities in the myocardium were based on 3% uptake for 4 mCi ^{201}Tl , multiplied by a factor 10 to enable measurements at limit contaminations (15 days after ART) in less than 36 h (32×3319 s) of uninterrupted scanner availability.

Data was acquired in a 180° study on a dual-headed Forte scanner equipped with LEHR collimators (see “Simulations of a digital thorax phantom”). Emission data was acquired on a 128×128 matrix (with a pixel size of 4.664 mm) for the $72 \pm 10\%$ and $167 \pm 10\%$ photopeak window in 64 projection views. The acquisition times are adapted to the decay rate to represent equal activity (cf.

Table 2). Projections representing the data acquired in both photopeak windows, as well as in each window separately, are stored for further reference. Attenuation correction was performed by using two scanning line sources containing ^{153}Gd that acquired transmission data in a moving electronic mask for the $100 \text{ keV} \pm 10\%$ energy window during 199 s for the reference scan and during 40 s for each of the 64 projection views. The latter were corrected for downscatter of 167 keV photons using an overlapping $100 \text{ keV} \pm 10\%$ energy window outside the electronic moving window [25].

The emission data respectively acquired in the low-energy photopeak and in the two photopeaks, simultaneously, were both reconstructed by ten OSEM iterations of eight subsets, thereby, applying attenuation correction and decay correction. No resolution recovery nor scatter correction was applied. Butterworth filtering (order 5; cutoff, 0.65) was performed as implemented by the scanner manufacturer: on the projections before reconstruction, on the forward projected data and before back-projecting during each iteration. Because of the large amount of noise, the high energy photopeak was reconstructed separately by 20 MLEM iterations with Butterworth filtering, attenuation and decay correction.

Analysis of the contrast was performed using circumferential planes. As shown in Fig. 3c, such planes are constructed by projecting the maximum count circumferential profiles onto a rectangular plane [26, 27] instead of projecting onto a polar coordinate system to produce a Bull’s eye. The relative contrast $C_r = |l - b|/b$ was defined where l is the average pixel value in the two cold defects, and b is the average pixel value in a reference region. The regions of interest for the defects have the size of the full defect and are centered at the minimum pixel value within each defect, whereas the reference region, b , is chosen in the myocardium outside the lesion as illustrated on Fig. 3d.

Results

Validation of Monte Carlo simulator

Figure 4 shows the result of the validation experiment described in “Validation of Monte Carlo simulator.” A good agreement between the measured and simulated energy spectrum in air can be concluded from Fig. 4a, which demonstrates both spectra at ART. Moreover, as in Fig. 4b, the full width at half maximum of the LSFs in air for the 167 keV photopeak matches and also the septal penetration tails of the measurement are accurately mimicked by the simulations.

Figure 5 shows a detailed analysis of a ^{201}Tl energy spectrum simulated with GATE, demonstrating a contam-

Table 2 Range of experimental contamination levels

Acquisition date	^{200}Tl (%)	^{202}Tl (%)	Total (%)	Seconds/angle
2 days early	0.39	0.17	0.56	60
ART	0.17	0.24	0.41	94
Half shelf-life	0.03	0.49	0.52	238
End of shelf-life	0.01	0.82	0.83	467
US limit	0.00	2.78	2.78	3319

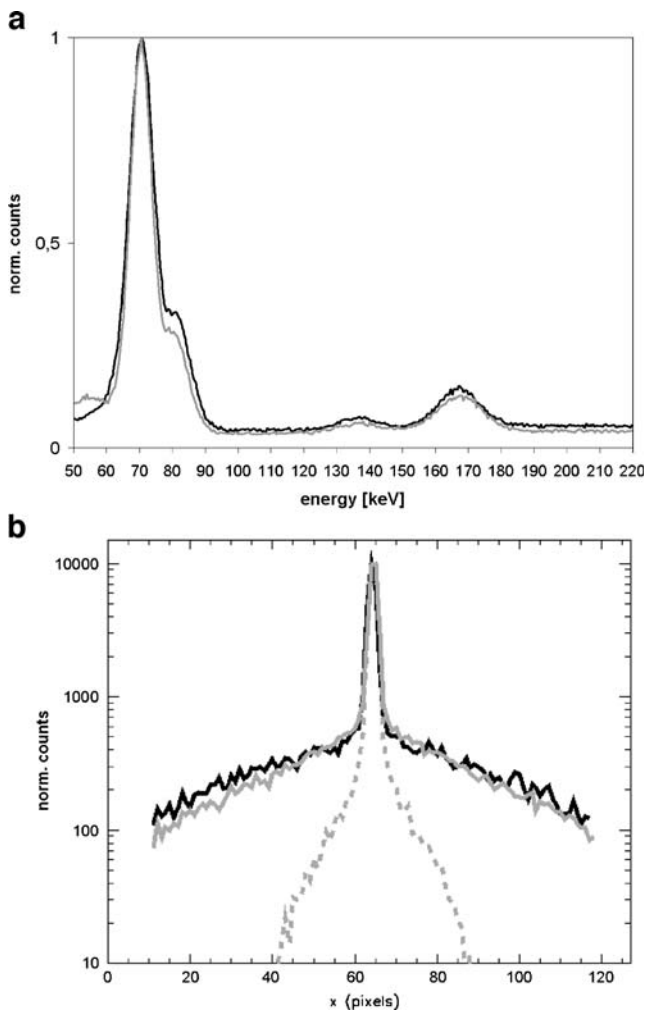
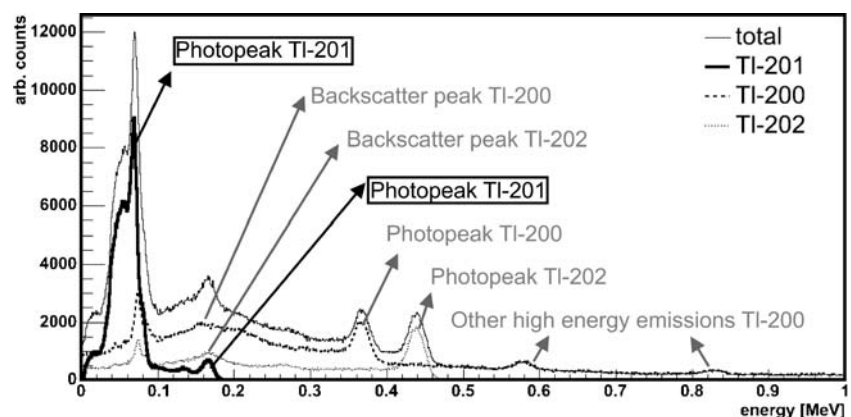


Fig. 4 Validation of the GATE Monte Carlo simulator: **a** measured and simulated energy spectrum with measurement (—) and simulation (---), **b** line spread functions for the 167 keV window with measurement (—), simulation (---) and simulation without contamination (----)

ination by 1% of ^{200}Tl and 1% of ^{202}Tl . It is also shown in Fig. 5 that the bias under the photopeaks of interest originates from the contaminants and is more particularly caused by septal penetration and downscatter of higher

Fig. 5 Simulated total (—) spectrum of a digital thorax phantom acquired on high-resolution collimators and filled with ^{201}Tl (—), which is contaminated by 1% ^{200}Tl (----) and 1% ^{202}Tl (.....). Note that this spectrum is plotted versus an energy scale that is extended beyond the clinical settings (0–200 keV) to better illustrate the origin of the bias under the ^{201}Tl photopeaks of interest



energy photons. This effect was already reported for other isotopes such as ^{123}I [28]. These high energy photons are mainly the 439 keV photons that have a branching ratio of 91% in the ^{202}Tl decay scheme and also the 368 keV photons from ^{200}Tl , resulting out of a 87% branching ratio. ^{200}Tl also has multiple other high-energy contributions in addition to its main photopeak, which could enhance the specific impact of ^{200}Tl over ^{202}Tl . Finally, it should be noted that the backscatter peak of the 439 and the 368 keV photons falls at 161.5 and 150.8 keV, respectively (Klein–Nishina), which is exactly within the 167 keV photopeak ($\pm 10\%$).

Quantitative analysis of the contaminations

Figure 6a shows the level of contamination for the two photopeak windows in three different regions (see “Simulations of a digital thorax phantom”) at ART, whereas Fig. 6b shows equivalent results 3 days after that date (half shelf-life). Generally, the amount of the contamination is larger in the 167-keV window given the lower abundance of that photopeak (10% 167 keV gammas compared to 70% for ± 72 keV X-rays). In this section, contamination by 1% of ^{200}Tl and ^{202}Tl each is simulated (see “Simulations of a digital thorax phantom”).

If the full active detector area is considered, then only 58% of all detections at ART in the 72-keV photopeak originate back to ^{201}Tl , whereas 29% and 12% of all photons comes from ^{200}Tl and ^{202}Tl , respectively. For the 167 keV photopeak window, this tendency is far more pronounced, as 62% of the photons detected in this photopeak window are the result of ^{200}Tl decay and 27% the result of ^{202}Tl . Accordingly, at ART, only 10% of all detections in the 167 keV photopeak window actually result from ^{201}Tl . As septal penetration has a broad spatial response, it is anticipated that these figures will improve if only the myocardial envelope is considered instead of the full active detector area. At ART, 71% of all detections result from ^{201}Tl in the 72-keV photopeak for the

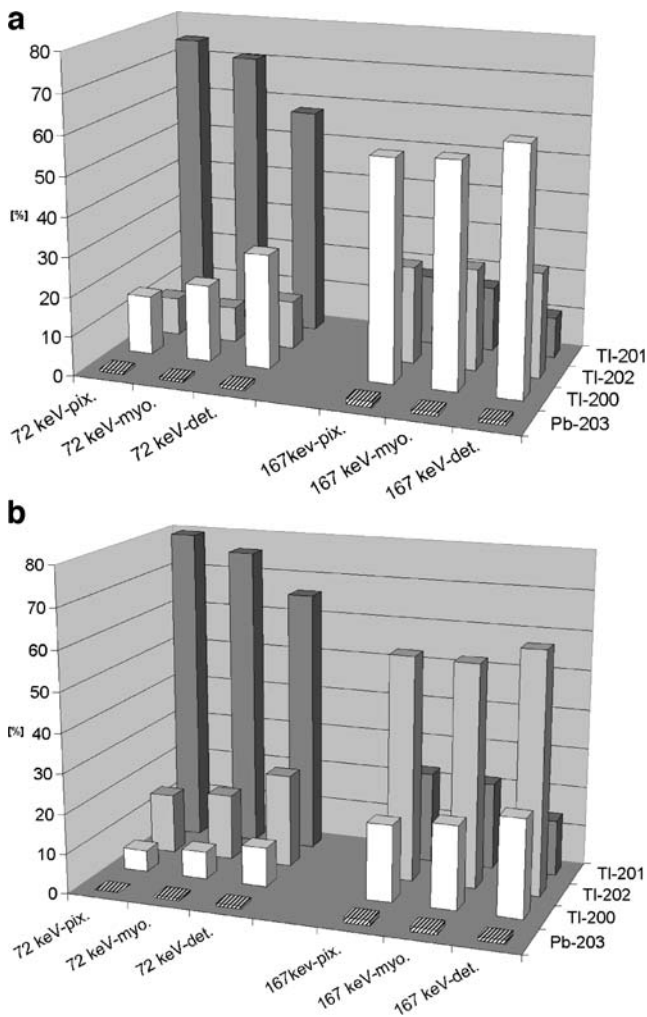


Fig. 6 Procentual contribution of ^{201}Tl and all contaminants for three regions and two energy windows **a** at activity reference time and **b** 3 days later (half shelf-life). Results for the 72-keV photopeak window are shown on the *left* and for the 167-keV photopeak window on the *right*. The *x*-axis differentiates between three different spatial regions: a central zone (*pix*), an envelope of the myocardium (*myo*) and the full detector (*det*). The *y*-axis indicates the four contaminant labels

myocardial envelope, whereas this is 16% for the 167 photopeak. At ART, most contaminations originate back to ^{200}Tl (20% and 57% of all detections, respectively, for the 72 and 167 keV photopeak), whereas this is fully inverted 3 days later when ^{202}Tl is the dominating contaminant (17% and 56% of all detections for the 72 and 167 keV photopeak, respectively). This effect is due to the large difference in half-lives as was already illustrated in Fig. 1. When the analysis is performed at pixel level for the central zone at ART, then 75% of all detections in the 72-keV window come from ^{201}Tl , but this number is still only 18% for the 167-keV photopeak.

Figure 7a illustrates the total contamination levels at ART detected in the 72 and 167 keV photopeak in the

myocardial envelope for both a LEHR and a LEGP collimator. The total contamination is slightly decreased when a general purpose collimator is used: Down to 22% contamination for the 72 keV window and 75% for the 167 keV window, whereas this was 29% and 84% for the high-resolution collimator.

Figure 7b, on the other hand, demonstrates that the contamination increases to 32% in the 72 keV window and to 85% in the 167-keV window for a larger-sized patient (on the high-resolution collimator).

Contrast deterioration

Figures 8, 9 and 10 show the results of the longitudinal measurements discussed in “Measurements.” For the data acquired in the high photopeak, the relative contrast of the inferior lesion and the average over both the lesions is plotted in Fig. 8a versus the contamination level, expressed in thallous (^{201}Tl) chloride shelf-life. Figure 8b–d shows the vertical long-axis views for three separate measure-

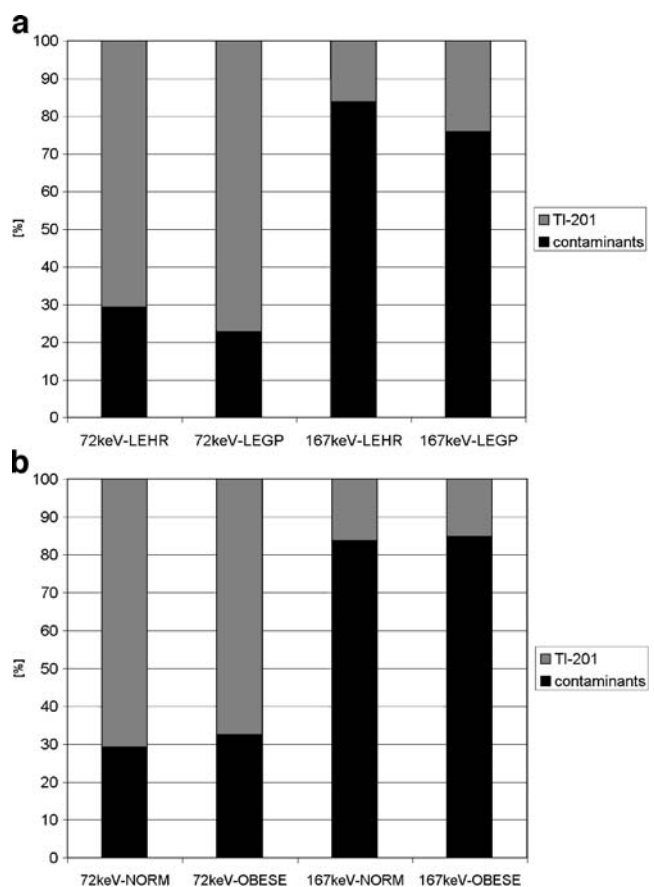


Fig. 7 Summary for the myocardial zone of interest: contribution (in terms of percentage) of all contaminants in both photopeak windows (72 and 167 keV) at activity reference time **a** for a LEHR and a LEGP collimator with a normal sized patient, **b** for a normal and a large patient acquired on a LEHR collimator

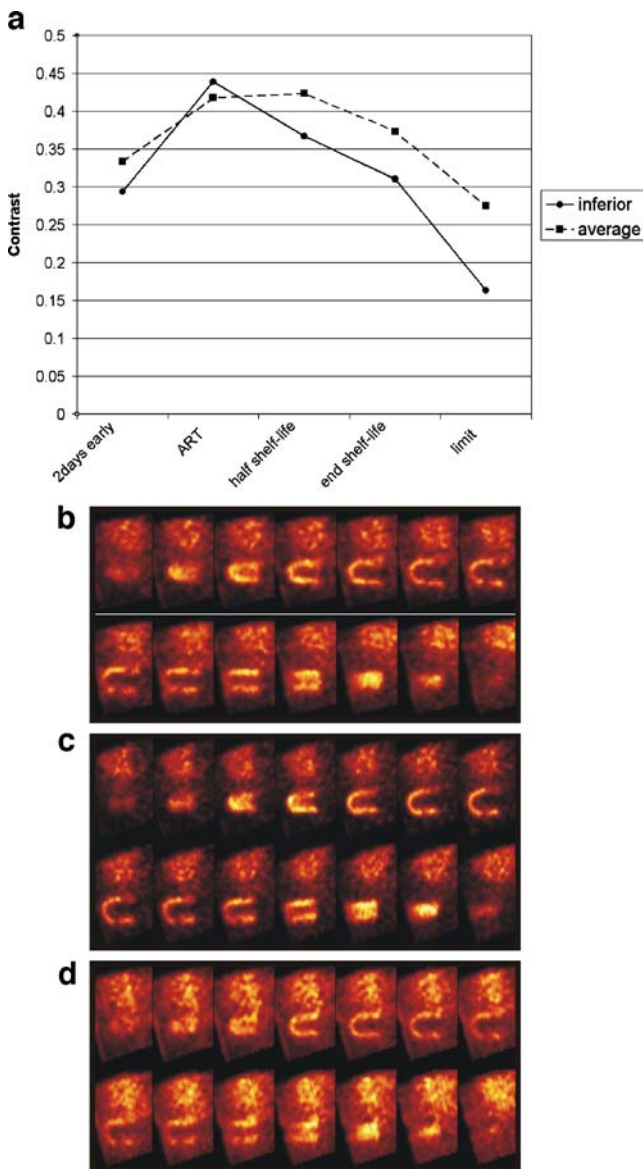


Fig. 8 Data acquired in the high photopeak window (167 keV): **a** contrast of the inferior lesion (—) and the contrast averaged over the inferior and the anterior lesion (---); **b** vertical long axis views of acquisitions performed 2 days early, **c** as **b** at activity reference time, **d** as **b** for the maximal allowed amount of contamination (according to US regulations)

ments in the 167 keV window: 2 days before ART, at ART and when the US contamination limit is reached. From Fig. 8a, it is shown that the contrast reaches a maximum around ART. For the inferior lesion, the contrast is 33% lower 2 days early because of an increased ^{200}Tl contamination, 17% and 29% lower at half and at the end of the shelf-life respectively, because of an increased ^{202}Tl contamination. This value even rises up to 63% when the US limit is reached. It can also be concluded that the contrast of the inferior lesion is generally lower compared to the average over both the inferior and the anterior lesion.

Figure 8b and d illustrate by comparison with Fig. 8c that the spatial response of the main contaminants is very broad, as both emit high-energy photons that penetrate the collimator or downscatter in the patient. Therefore, the inferior lesion is heavily influenced by the warm liver. As the branching ratio of the 167 keV emissions is only 10% compared to 70% for the X-rays in the 72 keV window, the main question remains whether these previous findings also influence imaging if both photopeaks are acquired simultaneously (as is often done in clinical practice).

Figure 9 shows similar results as Fig. 8 but for data acquired over both photopeak windows. In general, contrast increases by summing both photopeak windows. From Fig. 9a, we conclude that the average relative contrast drops 15% 2 days early. Similarly, contrast decreased by

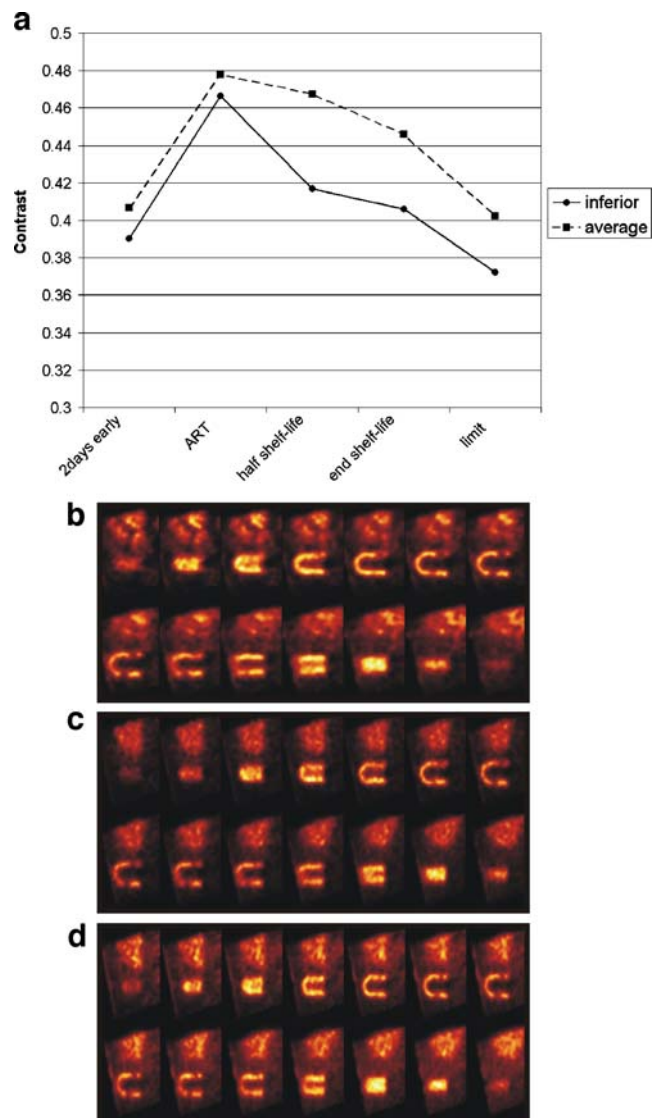


Fig. 9 Same as Fig. 8 but for data acquired in both photopeaks (72 and 167 keV) simultaneously

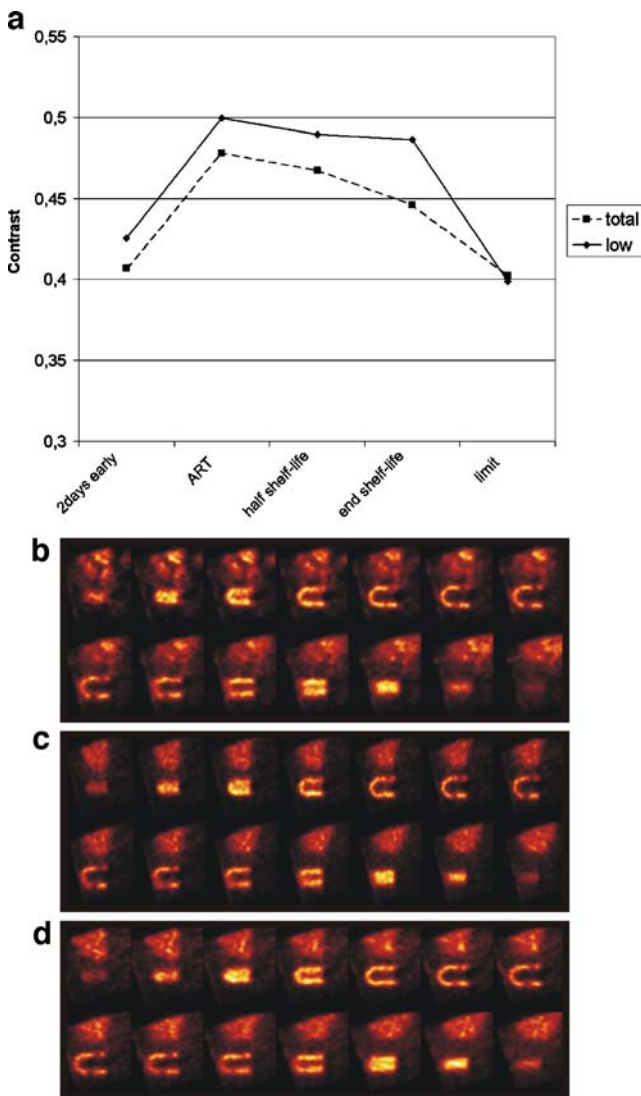
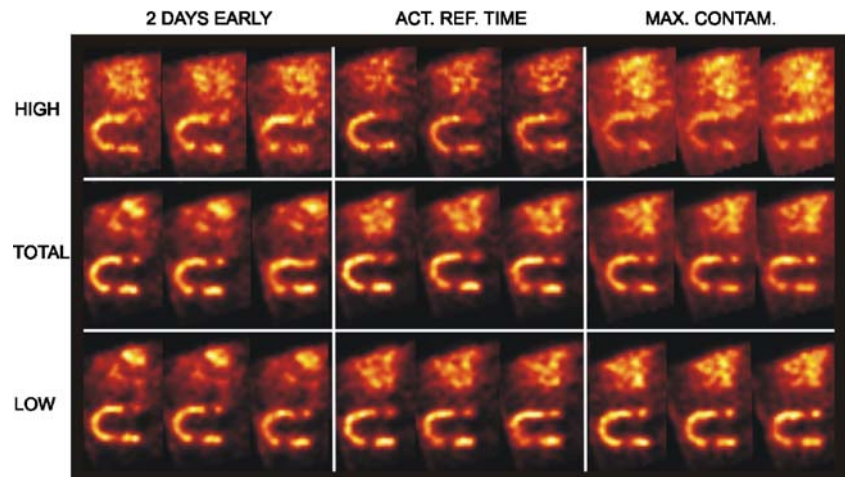


Fig. 10 Comparison of the contrast: **a** average contrast of the inferior and anterior lesion when only the low photopeak acquisition is reconstructed (—) and when both photopeak acquisitions are combined (---); **b** reconstructed vertical long axis views of the low photopeak acquisitions performed 2 days early, **c** as **b** at ART, **d** as **b** for the maximal allowed amount of contamination

Fig. 11 Three slices through the lesions for all configurations: 2 days early, at activity reference time, and at maximal contamination. Reconstructed vertical long axis views for the high, low and summed photopeak windows



2% at half the shelf-life of the thallous (^{201}Tl) chloride, by 7% at the end of the shelf-life and by 16% when the US contamination limit was reached. Moreover, Fig. 9b and d visually show that the contaminants' broad spatial response still deteriorates the inferior lesion significantly compared to Fig. 9c, even if data of both photopeaks is summed.

If only the low-energy photopeak acquisition would be reconstructed, then the contrast is generally higher compared to when both photopeaks are combined as can be seen from Fig. 10a. However, also the low-energy photopeak reconstructions are still significantly influenced by the contaminants as Fig. 10b–d show.

Figure 11 summarises the results for all the above configurations by showing three central slices through the two lesions on the reconstructed long axis views for every configuration: data acquired in the low, high and both photopeaks simultaneously 2 days early, at activity reference time and at maximal contamination.

Discussion

Monte Carlo simulations showed that approximately only two out of three photons in the 72 keV window are resulting from ^{201}Tl if the batch is contaminated by 1% contamination of ^{200}Tl and ^{202}Tl . For the 167-keV window, this number decreases to less than one out of five detected photons. This is because of the fact that the gamma camera's sensitivity is two orders of magnitude higher for the contaminants' high-energy photons, which penetrate the collimator or scatter in the patient. Similar values were found for both the high resolution as for the general purpose collimator used in nuclear cardiology practice, and an increase was concluded for large-sized patients, as the downscatter contribution from the high-energy photons increases in the latter case. Additionally, in many clinics,

photopeak windows of 30% are used, which would also increase this degrading effect.

Our measurements at several time stamps ranging from 2 days early up to the US contamination limit proved that the average relative lesion contrast in MPS imaging has a maximum around ART. These measurements also confirmed that relative contrast for inferior lesions close to a warm liver is generally lower as for anterior lesions because septal penetration and downscatter from high-energy photons has a broad spatial response.

Our measurements illustrated that scanning before the activity reference time is potentially more degrading than after ART, as the impact of ^{200}Tl appears to be larger because of its multiple high-energy emissions next to its main photopeak at 368 keV. This is clearly illustrated by Fig. 8a and 9a, where the decrease in contrast is steeper before than after ART. This hypothesis is confirmed by Fig. 5, where there is an equal amount of ^{200}Tl and ^{202}Tl and where the contribution to the bias under the photopeaks by ^{200}Tl is significantly higher.

A contrast-to-noise (CNR) analysis could show an even larger impact for the contaminations, as they add noise whilst lowering the contrast. At this stage, we varied contamination levels by measuring at different shelf-lives of the initial production batch. Therefore, we needed up to 36 h of uninterrupted scanner availability for high contamination measurements associated with low activity thallous (^{201}Tl) chloride. Accordingly, a CNR study is only feasible if the contamination is varied at the production plant. This will be a topic of further study involving extensive experiments.

The impact of the contaminants is most pronounced for the high-energy photopeak because of its lower branching ratio, but it also persists when both energy windows are combined. Moreover, it is shown that the highest contrast is achieved if only the low-energy photopeak acquisition is reconstructed. This renders the usage of the high-energy photopeak and its window settings questionable. Previously, this second photopeak capturing a small percentage of the emitted photons was considered important because the Compton scatter for photons at 167 keV and attenuation are much less as for photons at 72 keV. These factors increase the spatial information content of this second window. However, the findings in the present work illustrate that contamination levels of the thallous (^{201}Tl) chloride production tremendously degrade the information content of this window.

If both windows are to be acquired, correction for the effect is expected to improve contrast and quantitative accuracy. We, therefore, propose two potential solutions hereafter. Because the image degrading effect of these contaminations is mainly caused by septal penetration and downscatter of high-energy photons, resulting in detections with low spatial information content, two additional energy

windows at, for instance, 100 and 200 keV, can be acquired to correct for this persistent bias. This option is hampered by the fact that not that many clinical systems allow for acquisition with multiple and overlapping energy window. Another possibility is to counteract this effect by using a model-based correction during iterative reconstruction [29, 30]. Further research is required to investigate the accuracy and noise properties of different correction methods.

Throughout the previous results, it became clear that the current regulations on the contamination levels (3–5%) may be one order of magnitude too high and may need to be reconsidered. Also, a shelf-life of 7 days as claimed by many manufacturers is doubtful although usage at that date does not occur often in clinical practice due to the decay of ^{201}Tl . On the other hand administration up to 4 days before ART occurs readily and is even more degrading. This may need to be avoided as much as possible unless very high quality Thallous (^{201}Tl) Chloride is available.

Conclusion

We showed that the effect of even very low level contamination of ^{200}Tl and ^{202}Tl significantly impacts Thallous (^{201}Tl) Chloride images due to their inherent high energy photon emissions for which the gamma camera is much more sensitive.

We demonstrated that the currently well accepted maximum contamination levels could turn the acquisition of the 167 keV photopeak useless. The high contamination level and degradation of images prompts for reconsidering expiration dates and production methods, as well as the clinical practice of timing patient scans before the activity reference date.

Acknowledgment The authors thank Geert Ensing and Mark Konijnenberg (Tyco Healthcare/Mallinckrodt) Leonie Rijks (GE Healthcare) and Pascal Bartkowiak (Schering) for providing details on their production of thallous (^{201}Tl) chloride. The work of S.S. is supported by the Fund for Scientific Research, Flanders (FWO). The work of T.D.W. is supported by the Dutch Science and Technology Foundation (STW) by grant UGT.6069. The work of I.L. is supported by Ghent University, and the work of F.B. is supported by the Medical Counsel of the Dutch Organization for Scientific Research by grant 917.36.335. The contents are solely the responsibility of the authors and do not necessarily represent the official view of the sponsoring agencies.

References

1. Travin M, Bergmann S. Assessment of myocardial viability. *Semin Nucl Med.* 2005;35(1):2–16.
2. Germano G, Erel J, Kiat H, Kavanagh P, Berman D. Quantitative LVEF and qualitative regional function from gated ^{201}Tl perfusion SPECT. *J Nucl Med.* 1997;38(5):749–54.

3. Kelion A, Anagnostopoulos C, Harbinson M, Underwood S, Metcalfe M, British Nuclear Cardiology Society. Myocardial perfusion scintigraphy in the UK: insights from the British Nuclear Cardiology Society Survey 2000. *Heart* 2005;91(Suppl IV):2–5.
4. Gaim S, Weinrich R, Ollig H. Production of ^{201}Tl and ^{203}Pb via proton induced nuclear reactions on nuclear thallium. *Appl Radiat Isotopes*. 1978;30:85–95.
5. Bonardi M, Groppi F, Birattari C. A rapid improved method for gamma-spectrometric determination of ^{202}Tl impurities in [^{201}Tl]-labelled radiopharmaceuticals. *Appl Radiat Isotopes*. 2002;57:647–55.
6. United States Pharmacopoeial Convention. Thallous chloride injection. *United States Pharmacopeia* 2006;29:2108.
7. European Directorate for the Quality of Medicines. Thallous [^{201}Tl] chloride injection. *European Pharmacopeia* 2005;1:867.
8. British Pharmacopeia Commission. Thallous [^{201}Tl] chloride injection. *British Pharmacopeia* 2005;3:3088.
9. Thomas S, Stabin M, Castronovo F. Radiation-absorbed dose from ^{201}Tl -thallous chloride. *J Nucl Med*. 2005;46(3):502–8.
10. Bergamini C, Marengo M, Laudicina L, Mazzotti G, Dondi M. Estimation of radiation dose produced by impurities in nuclear medicine studies using ^{201}Tl chloride. *La Radiologia medica* (Torino). 1986;72(9):656–9.
11. Blachardon E, Challeton-de Vathaire C, Boisson P, Martin J-C, Cassot G, Herbelet G, et al. Long term retention and excretion of ^{201}Tl in a patient after myocardial perfusion imaging. *Radiat Prot Dosim*. 2005;113(1):47–53.
12. Stabin M, Brill B. Physics applications in nuclear medicine: organization and progress. *J Nucl Med*. 2006;47:22N–7N.
13. Groch M, Lewis G. ^{201}Tl : scintillation camera imaging considerations. *J Nucl Med*. 1975;17(2):142–5.
14. Saegusa K, Fukushi M, Katoh Y, Saitoh H, Irifune T. Gamma-ray spectra of ^{201}Tl -radiopharmaceuticals with a scintillation camera—crosstalk of contaminating nuclides of ^{200}Tl and/or ^{202}Tl onto ^{201}Tl -photopeaks. *Radioisotopes*. 1990;39(6):255–60.
15. Agnostelli S, Allison J, Amako K, et al. Geant4: a simulation toolkit. *Nucl Instrum Methods A*. 2003;506:250–303.
16. Bielajew A, Hirayama H, Nelson W, Rogers D. History, overview and recent improvements of EGS4 Tech. Rep. Ottawa, Canada: National Research Council; 1994.
17. Briesmeister J. MCNP—a general Monte Carlo N-particle transport code. Tech. Rep. Los Alamos National Laboratory, Los Alamos, NM, USA. 1993.
18. Jan S, Santin G, Strul D, et al. GATE: a simulation toolkit for PET and SPECT. *Phys Med Biol*. 2004;49:4543–61.
19. Assié K, Gardin I, Vera P, Buvat I. Validation of the Monte Carlo simulator GATE for ^{111}In imaging. *Phys Med Biol*. 2005;50:3113–25.
20. Lazaro D, Buvat I, Loudos G, et al. Validation of the GATE Monte Carlo simulation platform for modelling a CsI(Tl) scintillation camera dedicated to small-animal imaging. *Phys Med Biol*. 2004;49:271–85.
21. Staelens S, Strul D, Santin G, et al. Monte Carlo simulations of a scintillation camera using GATE: validation and application modelling. *Phys Med Biol*. 2003;48:3021–42.
22. Tsui B, Zhao X, Gregoriou G, Lalush D, Frey E, Johnston R, et al. Quantitative cardiac SPECT reconstruction with reduced image degradation due to patient anatomy. *IEEE Trans Nucl Sci*. 1994;41:2838–44.
23. LaCroix K, Tsui B, Hasegawa B. A comparison of 180 degrees and 360 degrees acquisition for attenuation-compensated ^{201}Tl SPECT images. *J Nucl Med*. 1998;39(3):562–74.
24. Kadmas D, Frey E, Tsui B. Simultaneous $^{99\text{m}}\text{Tc}/^{201}\text{Tl}$ SPECT imaging with model-based compensation for cross-contaminating effects. *Phys Med Biol*. 1999;44(7):1843–60.
25. Gagnon D, Tung C, Zeng L, Hawkins W. Design and early testing of a new medium-energy transmission device for attenuation correction in SPECT and PET. *Proc. IEEE Med Imaging Conf*. 1999;3:1349–53.
26. Germano G, Kavanagh P, Waechter P, et al. A new algorithm for the quantitation of myocardial perfusion SPECT: technical principles and reproducibility. *J Nucl Med*. 2000;41:712–9.
27. de Puey E, Garcia E, Berman D. *Cardiac SPECT imaging*. 2nd ed. Philadelphia, PA: Lippincott Williams and Wilkins; 2001.
28. Dobbeleir A, Hambye A-S, Franken P. Influence of high-energy photons on the spectrum of ^{123}I with low and medium-energy collimators: consequences for imaging with ^{123}I labelled compounds in clinical practice. *Eur J Nucl Med Mol I*. 1999;26:655–8.
29. Staelens S, de Wit T, Beekman F. Ultra-fast SPECT simulation with combined convolution based forced detection and efficient septal penetration modeling [abstract]. *J Nucl Med*. 2006;47(Suppl):198P.
30. Staelens S, de Wit T, Beekman F. Fast hybrid SPECT simulation including efficient septal penetration modelling (SP-PSF). *Phys Med Biol*. 2007;52:3027–43.